Short Article

Developmental Cell

The *Xenopus* spindle is as dense as the surrounding cytoplasm

Graphical abstract

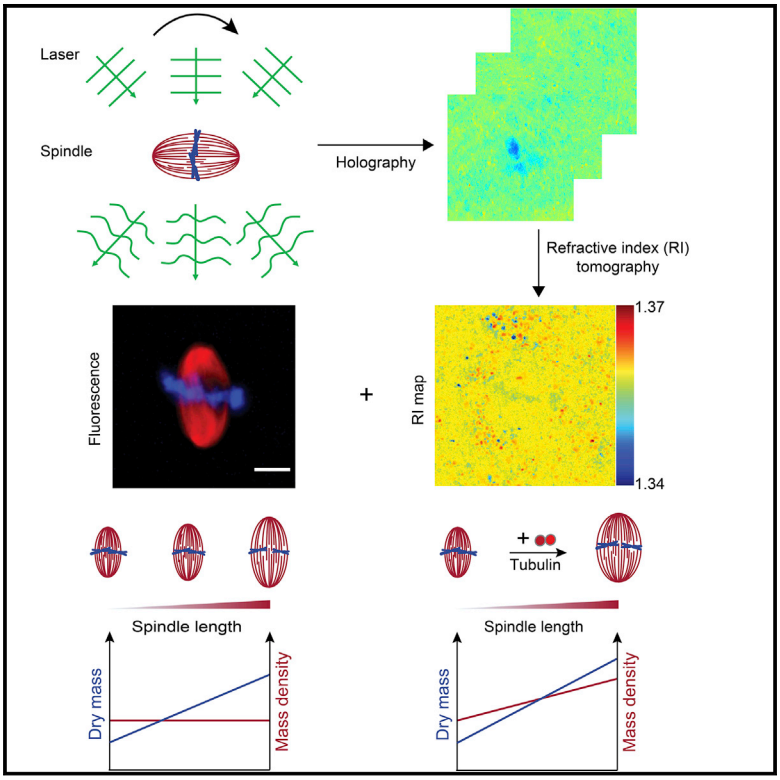

Authors

Abin Biswas, Kyoohyun Kim, Gheorghe Cojoc, Jochen Guck, Simone Reber

Correspondence

simone.reber@iri-lifesciences.de

In brief

The mitotic spindle has previously been described as a dense protein-rich phase of the cytoplasm. Using correlative fluorescence and quantitative phase imaging, Biswas et al. show that *Xenopus* spindles have the same mass density as the surrounding cytoplasm. Tuning microtubule nucleation and dynamics by supplementing tubulin alters spindle geometry and density.

Highlights

- ODT maps the mass density distribution in spindles
- *Xenopus* spindles are as dense as the surrounding cytoplasm
- Mass density is stiffness invariant in mechanically distinct spindle regions
- Spindle mass density can be modulated by tuning microtubule nucleation and dynamics

Biswas et al., 2021, Developmental Cell *56*, 967–975
April 5, 2021
https://doi.org/10.1016/j.devcel.2021.03.013

CellPress

Developmental Cell

CellPress

Short Article

The *Xenopus* spindle is as dense as the surrounding cytoplasm

Abin Biswas,[1,2,6] Kyoohyun Kim,[2,3,6] Gheorghe Cojoc,[3] Jochen Guck,[2,3,4] and Simone Reber[1,5,7,*]
[1]IRI Life Sciences, Humboldt-Universität zu Berlin, 10115 Berlin, Germany
[2]Max-Planck-Institute for the Science of Light, 91058 Erlangen, Germany
[3]BIOTEC, Technische Universität Dresden, 01307 Dresden, Germany
[4]Cluster of Excellence Physics of Life, Technische Universität Dresden, 01307 Dresden, Germany
[5]University of Applied Sciences Berlin, 13353 Berlin, Germany
[6]These authors contributed equally
[7]Lead contact
*Correspondence: simone.reber@iri-lifesciences.de
https://doi.org/10.1016/j.devcel.2021.03.013

SUMMARY

The mitotic spindle is a self-organizing molecular machine, where hundreds of different molecules continuously interact to maintain a dynamic steady state. While our understanding of key molecular players in spindle assembly is significant, it is still largely unknown how the spindle's material properties emerge from molecular interactions. Here, we use correlative fluorescence imaging and label-free three-dimensional optical diffraction tomography (ODT) to measure the *Xenopus* spindle's mass density distribution. While the spindle has been commonly referred to as a denser phase of the cytoplasm, we find that it has the same density as its surrounding, which makes it neutrally buoyant. Molecular perturbations suggest that spindle mass density can be modulated by tuning microtubule nucleation and dynamics. Together, ODT provides direct, unbiased, and quantitative information of the spindle's emergent physical properties—essential to advance predictive frameworks of spindle assembly and function.

INTRODUCTION

The mitotic spindle is a classic example of a self-organizing organelle, where hundreds of different molecules interact with continuous flux of material and constant dissipation of energy to maintain a dynamic steady state (Dumont and Mitchison, 2009; Reber and Hyman, 2015; Elting et al., 2018). While the last decades were instrumental in identifying most of the molecules essential to spindle function, there remains a major gap in our understanding of how different molecular processes collectively give rise to the spindle's mesoscale material properties.

Recent advances combining *in vitro* reconstitution and concepts of soft matter physics have established first quantitative and predictive frameworks explaining how spindle size and shape arise and are maintained (Reber et al., 2013; Brugués and Needleman, 2014; Oriola et al., 2020). *Xenopus* spindles, for example, have been described as droplets of liquid-crystals with constant microtubule density (Reber et al., 2013; Brugués and Needleman, 2014), where microtubule mass determines size. This is in agreement with the recent concept of liquid-liquid phase transition separating membraneless organelles from the nucleo- and cytoplasm (Hyman et al., 2014). Furthermore, spindle centrosomes have been described as condensates that nucleate microtubules by concentrating tubulin (Woodruff et al., 2017). Similarly, acentrosomal spindles in oocytes possess liquid-like meiotic spindle domains where critical spindle proteins localize (So et al., 2019). Moreover, spindle proteins such as BugZ and TPX2 (Jiang et al., 2015; King and Petry, 2020) have been shown to form droplets *in vitro* and to specifically concentrate tubulin. For BugZ, it has been suggested that a condensed spindle phase could encourage transition-state-limited reactions during spindle assembly (Woodruff, 2018). While local crowding builds a chemically and mechanically distinct micro-environment around chromatin during mitosis, it remains unknown whether the spindle is an overall denser phase when compared with the surrounding cytoplasm. A general challenge that remains is how to parameterize the degree of crowding (Mitchison, 2019) not only in the cellular environment but also in *in vitro* reconstitutions.

The mass density of a material generally scales with its refractive index (RI). In most biological materials, the RI is linearly proportional to the mass density of macromolecules and can thus be used to quantify its degree of condensation (Zhao et al., 2011; Zangle and Teitell, 2014). Furthermore, a sample's mass density can be used to calculate its dry mass or the total amount of non-aqueous material such as its protein content (Kim et al., 2016; Kim and Guck, 2020). Optical diffraction tomography (ODT) is an interferometric phase imaging technique (Sung et al., 2009), which provides quantitative three-dimensional

(3D) RI distributions without the need of exogenous labels (Kim et al., 2016; Kim and Guck, 2020). ODT has been successfully used to study both phase separation (Guillén-Boixet et al., 2020) and transition (Abuhattum et al., 2018). While traditional quantitative fluorescence microscopy methods only allow us to observe what we label, ODT provides unbiased quantitative information of a sample *in toto*. Additionally, ODT imaging helps overcome caveats of fluorescence imaging including fluorophore quenching, photobleaching, phototoxicity, and non-uniform fluorophore labeling (Kim et al., 2018). Only recently, it has been used to determine protein concentration in condensates with higher precision than traditional fluorescence-based methods (McCall et al., 2020).

In this study, we used a correlative fluorescence-ODT setup to quantitatively measure mass density and dry mass of *Xenopus* spindles reconstituted in egg extracts. We show that—contrary to common expectation—steady-state spindles have the same mass density as the surrounding cytoplasm. Further, we find that the mass density is not correlated with stiffness in mechanically distinct spindle regions. In agreement with a microtubule mass balance model (Reber et al., 2013), the average mass density of spindles is independent of spindle length while the dry mass scales linearly with spindle length. In addition, we derive the dry mass of a typical *Xenopus* spindle to be ~300 pg. When increasing spindle size by supplementing tubulin, mass density increased. This suggests multiple molecular mechanisms of microtubule nucleation and dynamics at work. Collectively, this study provides insights into so far unmeasured key biophysical spindle properties essential for spindle function.

RESULTS

Xenopus spindles have the same mass density as the surrounding cytoplasm

The optical system used to image *Xenopus* egg extract spindles is an integrated setup for both epi-fluorescence microscopy and high-resolution ODT (Figure 1A) (Kim and Guck, 2020). This combination allows us to attribute specific molecular information via fluorescence to 3D RI measurements. In ODT, a 3D tomogram is reconstructed from multiple 2D phase images that are obtained upon illuminating the sample with various oblique angles (Figure 1B) (Kim et al., 2016). Surprisingly, *in vitro* reconstituted spindles could not be distinguished from the surrounding cytoplasm in the acquired ODT image. However, spindles and chromatin could be identified using fluorescent labeling (Figure 1C). Subsequently, we used fluorescence images to generate masks referred to as "cytoplasm," "spindle," and "chromatin" (Figure 1C) to measure the average RI of these regions of interest (ROI) in ODT images (Figure 1D). Since the RI of biological specimens is linearly proportional to the biomolecule concentration (Barer et al., 1953; Popescu et al., 2008; Zhao et al., 2011) (Figure S1A), ODT provides a direct quantitative readout of mass and density. ODT reliably provided RI values of known materials with minimal error (Figures S1B–S1E). Quantifying the mass density within the central spindle slice (inset Figure 1C, see STAR Methods for further details) from 320 different ROIs (5 ROIs each from 64 spindles) revealed that spindles (red circles, Figure 1D, 105 ± 0.4 mg/mL, mean ± SEM) had an identical mass density as the cytoplasm (yellow circles, Figure 1D, 105 ± 0.4 mg/mL, similar to the protein concentration measured in Groen et al., 2011), while chromatin had a lower mass density (blue circles, Figure 1D, 102 ± 0.6 mg/mL; $p_{cytoplasm,\ chromatin} < 0.0001$, d (effect size) $_{cytoplasm,\ chromatin} = 0.4$). To independently confirm the lack of contrast between spindles and surrounding cytoplasm, we resorted to optical trapping. Differences in the RI between an object and its surrounding medium can be used to trap and deform the object (Guck et al., 2001). While experiments with optical stretchers (OSs) have been routinely used on a cellular level (Guck et al., 2005; Lautenschläger et al., 2009; Huster et al., 2020), they have not been performed in *in vitro* reconstituted systems. We thus used a custom-built OS setup (Figure S2A) designed for *Xenopus* egg extract experiments. While we were able to trap and stretch membrane-bound organelles (Figure S2B), we were unable to exert any optical force on spindles (Figure S2C). This independently supports the ODT result in that there is no significant difference between the RI of *Xenopus* spindles and the surrounding cytoplasm. For some spindles, we noticed a high-RI rim (Figure S3C), which we identified to be membranes (Figure S3B). Indeed, non-continuous membrane-rich regions have previously been described around spindles of *Drosophila melanogaster* S2 and HeLa cells and mouse oocytes (Dalton and Carroll, 2013; Schweizer et al., 2015). Taken together, we established a correlative analysis based on RI and fluorescence images, which allows us to calculate the mass density of reconstituted spindles in *Xenopus* egg extracts. Although the spindle is often described as a dense and crowded environment (Carlini et al., 2020), *Xenopus* spindles have the same mass density as the surrounding cytoplasm.

Mass density is stiffness invariant in mechanically distinct spindle regions

The *Xenopus* spindle exhibits viscoelastic properties, which depend on the timescale and direction of applied forces (Shimamoto et al., 2011). In addition, spindle mechanics varies as a function of local architecture (Takagi et al., 2019). We thus asked whether the spindle mass density differs depending on position within the spindle and microtubule architecture. We defined three zones within a *Xenopus* spindle (based on Takagi et al., 2019): the spindle poles (Figure 2A, green), the spindle middle (Figure 2A, blue), and the spindle equator (Figure 2A, red). These parts of the spindle have different dynamic moduli (Takagi et al., 2019) with the pole being the stiffest (2.4 ± 2.5 kPa), followed by the equator (1.5 ± 1.1 kPa) and the middle of the spindle (0.7 ± 0.4 kPa). Using the ODT setup, we were able to obtain the mass density distribution with high lateral spatial resolution (0.25 μm per pixel). Calculating the mass density from ODT images revealed that the spindle pole and middle parts had similar mass density values (pole: 94 ± 1.0 mg/mL, middle: 94 ± 1.1 mg/mL), while the equator had a significantly lower mass density (89 ± 1.2 mg/mL; $p_{pole,\ equator} < 0.001$, $d_{pole,\ equator} = 0.6$) (Figure 2B). While making measurements at the spindle equator, void space occupied by the DNA was carefully avoided to not bias the analysis. We expect that the mechanical response of the spindle to forces will depend on its elasticity, which in turn can scale with mass density. In material sciences, Ashby plots (Ashby, 2011) provide insight into such mechanofunctionality. We thus plotted the stiffness against mass density for the different spindle regions (Figure 2C). We find that mass density

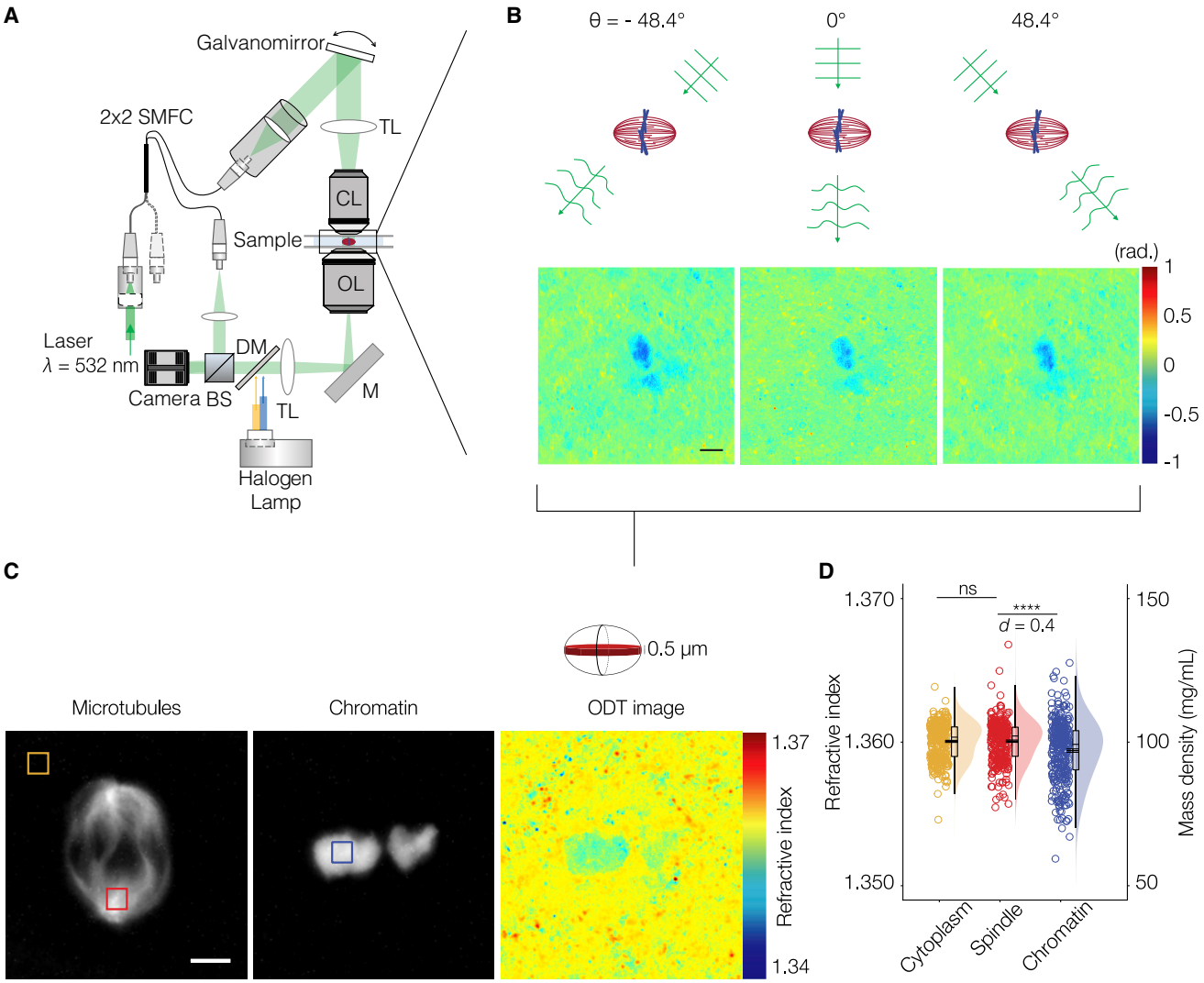

Figure 1. *Xenopus* spindles have the same mass density as the surrounding cytoplasm

(A) Optical setup used to obtain fluorescence and refractive index images of *Xenopus* spindles. SMFC, single mode fiber coupler; TL, tube lens; CL, condenser lens; OL, objective lens; M, mirror; DM, dichroic mirror; BS, beam splitter.

(B) Phase maps of a representative spindle illuminated at various angles. Scale bar, 10 μm.

(C) Fluorescence images showing microtubules (labeled with TAMRA-tubulin) and chromatin (labeled with Hoechst 33342) of the same spindle. The colored boxes represent regions of interest (5 μm × 5 μm) used for measuring the RI of cytoplasm, spindle, or chromatin (yellow, red, and blue boxes, respectively). Reconstructed ODT image of the spindle's central plane used for RI and mass density measurements.

(D) Average RI and mass density (mg/mL) of cytoplasm, spindle, and chromatin. Cytoplasm (yellow) 105 ± 0.4 mg/mL, spindle (red) 105 ± 0.4 mg/mL, chromatin (blue) 102 ± 0.6 mg/mL, $p_{cytoplasm,\ chromatin} < 0.0001$, Cohen's $d_{cytoplasm,}$ chromatin = 0.4. n = 320 ROIs from 64 spindles. Data are represented as mean ± SEM. Mann-Whitney test. Black bar and lines indicate mean and standard error of mean. Box and violin plot for each condition indicated, ns $p > 0.05$, ****$p < 0.0001$. See also Figures S1–S3.

does not correlate with stiffness (dynamic modulus) in *Xenopus* spindles. This is surprising and different from many engineering and biological materials (Wegst and Ashby, 2004) and underscores the need to better characterize and understand complex biological materials such as the spindle (see Discussion).

Spindle mass density correlates with microtubule density

On a coarse-grained level, spindles have been described as condensed phases of the cytoplasm with liquid-like properties (Reber et al., 2013; Brugués and Needleman, 2014). Consistently, spindles fuse, turn over, and recover their form upon perturbations (Gatlin et al., 2009; Takagi et al., 2013). An important parameter for the liquid-like picture to work is constant microtubule density. In such a scenario, an increase in microtubule mass leads to an increase in spindle size (Reber et al., 2013; Decker et al., 2018). Using fluorescence data, we measured the microtubule density along the spindle pole-to-pole axis (Figure 3A). The spindle middle and poles had similar microtubule densities (Figure 3B, red data points, pole: 3 ± 0.2 AU/μm^2, center: 3 ± 0.2 AU/

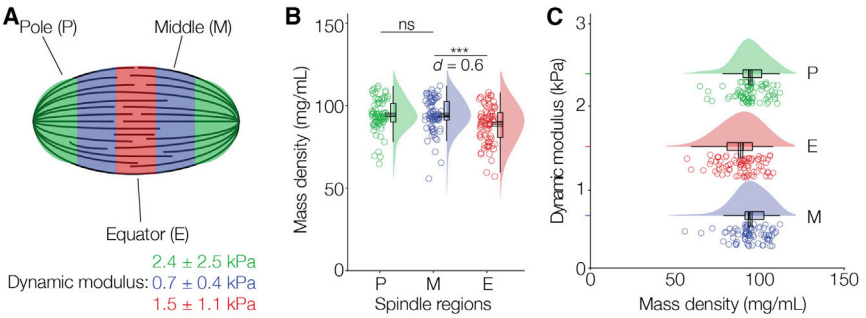

Figure 2. Mass density is stiffness invariant in mechanically distinct spindle regions

(A) Schematic representing three architecturally and mechanically distinct regions (Takagi et al., 2019) within spindles, spindle poles (green), middle of the spindles (blue), and spindle equator (red).

(B) Mass density of the three different regions. Spindle pole: 94 ± 1.0 mg/mL, spindle middle: 94 ± 1.1 mg/mL, and spindle equator: 89 ± 1.2 mg/mL, $p_{pole,\ equator} < 0.001$, Cohen's $d_{pole,\ equator} = 0.6$.

(C) Ashby plot of the median dynamic modulus of different spindle regions versus the corresponding mass density. Each circle represents the average value of an ROI (5 μm × 5 μm). n = 80 ROIs from 20 spindles. Data are represented as mean ± SEM. Mann-Whitney test. Black bar and lines indicate mean and SEM. Box and violin plot for each condition indicated, ns $p > 0.05$, ***$p < 0.001$.

μm^2), while the equator had a slightly lower microtubule density (2 ± 0.1 AU/μm^2). Calculating the mass density from the ODT images revealed that the spindle pole and middle parts had similar values (Figure 3B, black data points, pole: 95 ± 1.1 mg/mL, middle: 95 ± 1.0 mg/mL), while the equator had a slightly lower mass density (88.8 ± 1.2 mg/mL). These data imply that spindle mass density correlates with microtubule density. Next, we took advantage of the fact that spindles reconstituted in *Xenopus* egg extracts show a wide size distribution (Figure 3C, Grenfell et al., 2016). As predicted by the "liquid-crystal" analogy, microtubule density as assessed by fluorescence microscopy remained roughly constant (Figure 3D, 5 ± 0.2 AU/μm^2) independent of spindle length. Similarly, the average mass density was constant and independent of spindle length (Figure 3E, 97 ± 0.8 mg/mL). From the fluorescence and ODT data, we derived the total microtubule mass and the dry mass of spindles, respectively (see STAR Methods). Both parameters scaled linearly (R^2 = 0.6162 and 0.8447, respectively) with spindle length (Figure 3F). The dry mass of a *Xenopus* spindle with an average length of 32 ± 1.1 μm (n = 76 spindles) was calculated to be 290 ± 19 pg (see STAR Methods). These data support the idea that total microtubule mass sets spindle size, expanding the observation from total microtubule mass to total protein mass.

Increasing tubulin concentration increases spindle mass density and spindle circularity

Despite some heterogeneity in *Xenopus* egg extracts, spindle length is thought to reach an upper limit in extracts and in very large cells (Wühr et al., 2008; Crowder et al., 2015; Rieckhoff et al., 2020). Previous research has proposed tubulin, the fundamental building block of microtubules, as the limiting component to spindle length (Good et al., 2013). Indeed, recent work has shown that the addition of *Xenopus* tubulin to steady-state spindles increases total microtubule mass and thus spindle length (Hirst et al., 2020). Analogously, we assembled spindles and supplemented increasing concentrations of purified *X. laevis* tubulin (Figure 4A). Correlative fluorescence and ODT images of spindles were acquired and spindle length, microtubule density, and mass density were quantified. Adding tubulin to pre-assembled spindles resulted in significantly longer spindles (Figure 4B; wild type: 31 ± 1.3 μm, +2 μM: 40 ± 1.3 μm; $p_{WT,\ 2\ \mu M} < 0.0001$, $d_{WT,\ 2\ \mu M} > 1$, +4 μM: 47 ± 1.7 μm; $p_{WT,\ 4\ \mu M} < 0.0001$, $d_{WT,\ 4\ \mu M} > 1$) but importantly did not change the overall mass density of the cytoplasm (Figure S4A). Next, we calculated the total microtubule mass and dry mass of each wild type and tubulin-supplemented spindle (Figures S4B–S4D). As predicted by the mass balance model, the total microtubule mass and dry mass scaled linearly with spindle length. Upon adding 2 and 4 μM tubulin, the average spindle dry mass increased from 290 ± 26 to 540 ± 42 and 630 ± 44 pg (black dotted lines in Figures S4B–S4D), respectively. We next measured microtubule density, which revealed that tubulin-supplemented spindles had a higher overall microtubule density (Figure 4C; wild type: 5 ± 0.4 AU/μm^2, +2 μM: 6 ± 0.3 AU/μm^2; $p_{WT,\ 2\ \mu M} < 0.05$, $d_{WT,\ 2\ \mu M} = 0.7$ and +4 μM: 7 ± 0.3 AU/μm^2; $p_{WT,\ 4\ \mu M} < 0.0001$, $d_{WT,\ 4\ \mu M} > 1$). With increasing microtubule density, mass density increased (Figure 4D; wild type: 92 ± 1.1 mg/mL, + 2 μM: 95 ± 0.5 mg/mL; $p_{WT,\ 2\ \mu M} > 0.05$, $d_{WT,\ 2\ \mu M} = 0.6$ and + 4 μM: 96 ± 0.4 mg/mL; $p_{WT,\ 4\ \mu M} < 0.01$, $d_{WT,\ 4\ \mu M} = 0.9$). So far, microtubule density has been considered a robust spindle parameter, which remained constant even after spindle perturbations that significantly changed microtubule dynamics and spindle size (Reber et al., 2013; Decker et al., 2018; Rieckhoff et al., 2020). Why would an increase in tubulin concentration increase the spindle's mass density? Increasing tubulin concentration increases microtubule growth velocity (Gardner et al., 2011). Above a certain critical concentration, however, increasing tubulin concentration might in addition affect microtubule nucleation (Wieczorek et al., 2015). We therefore propose that the increase in mass density is due to the additional microtubule nucleation in the spindle bulk. Theoretical arguments (Reber et al., 2013; Brugués and Needleman, 2014) predict that modifying the spindle's nucleation profile will change both spindle length and shape. Indeed, spindles became more circular (Figure 4E; wild type: 0.74 ± 0.02, +2 μM: 0.79 ± 0.01, and +4 μM: 0.82 ± 0.01; see also Figures S4E and S4F) with increasing tubulin concentration. Together, our quantitative analyses suggest that increasing tubulin concentration increases spindle length and shape by increasing microtubule growth and nucleation.

DISCUSSION

Our correlative fluorescence-ODT setup allowed us to obtain molecular information and quantitatively measure mass density and dry mass in *Xenopus* spindles reconstituted in egg extracts. Although the spindle has previously been described as a

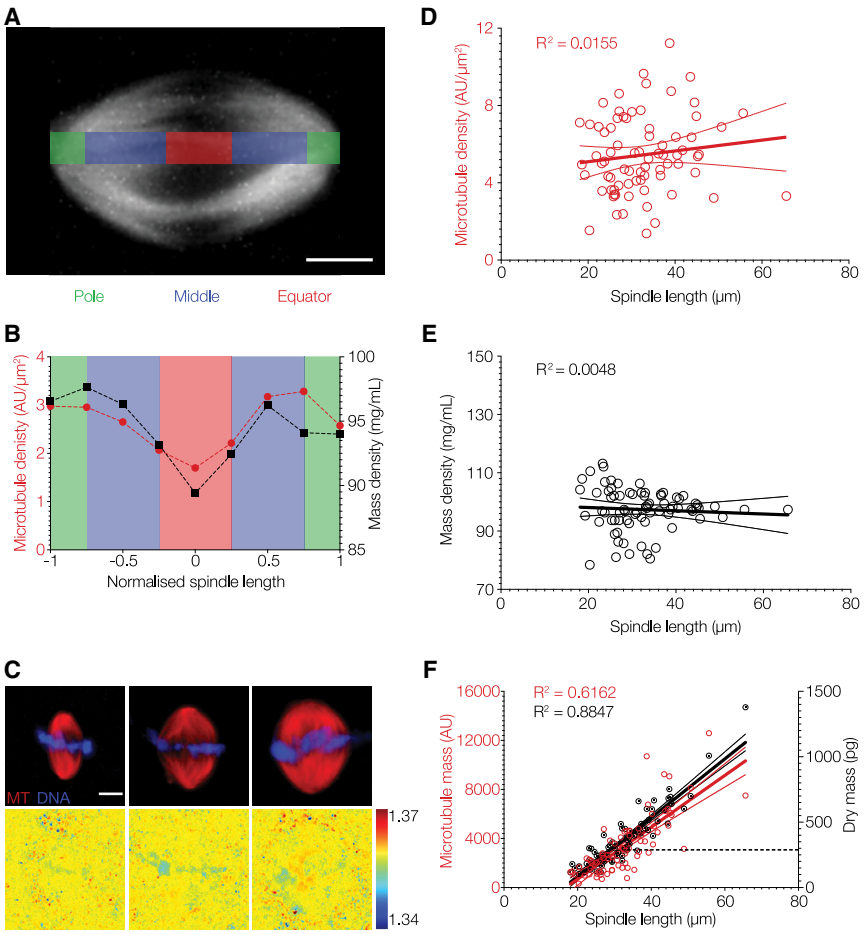

Figure 3. Spindle mass density correlates with microtubule density

(A) Fluorescence image of a representative *Xenopus* spindle. Microtubule and mass density were measured along the pole-pole axis (green: spindle poles, blue: spindle middle, red: spindle equator). Scale bar, 10 μm.

(B) Microtubule and mass density vary along the pole-pole axis. Circles and squares represent the average microtubule (red) and mass density (black), respectively. n = 36 spindles.

(C) Representative fluorescence images (top) and corresponding ODT images (bottom) of spindles of different sizes (red, microtubules; blue, DNA). Scale bar, 10 μm.

(D) Average microtubule density of 76 spindles showing natural length variation (20–70 μm).

(E) Average mass density of spindles in (D).

(F) Microtubule mass and spindle dry mass scale with spindle length. Each circle represents the microtubule mass (from fluorescence images) and the dry mass of one spindle. Dotted black line indicates the average dry mass of a wild-type *Xenopus* spindle (290 pg). Bold lines (D–F) indicate a linear fit of the data, and thin lines indicate the 95% confidence interval of the fitted function. R^2 value for each fit indicated.

condensed phase of microtubules and associated proteins, we show that spindles are physically not denser than the surrounding cytoplasm. Using our fluorescence-ODT setup, we further investigated the optical properties of mechanically and architecturally distinct spindle regions. While we did not find a correlation between previously measured dynamic moduli and spindle density, we observed a co-dependence between microtubule density and mass density. In wild-type spindles, microtubule density and mass density stay constant, independent of spindle length, while total microtubule mass and dry mass scale linearly with spindle length. Finally, by increasing the tubulin concentration in egg extracts, we propose that spindle length and mass density increase in response to increasing microtubule growth and nucleation.

In summary, we report that the spindle has the same mass density than the surrounding cytoplasm, but what is the physiological and functional significance? First, we would argue that on our way toward a systematic and quantitative understanding of mitotic spindle form and function, providing a direct, label-free, and quantitative measure of a key spindle material property is valuable in itself. Our mass and density measurements are essential to advance predictive frameworks. They can further inform or constrain current theoretical models of spindle size control (Good et al., 2013; Reber et al., 2013; Decker et al., 2018; Oriola et al., 2020; Rieckhoff et al., 2020). In addition, knowing the RI is helpful when characterizing sample-induced aberrations in super-resolution techniques such as STED and structured illumination. Finally, emerging optical methods such as Brillouin microscopy, where knowledge of density and RI is required to convert the measured Brillouin shift into a longitudinal modulus (Scarcelli et al., 2015; Prevedel et al., 2019; Schlüßler et al., 2020), will take advantage of our measurements to further explore the spindle's mechanical properties.

Second, the mass density we provide is a mesoscale material property. While the mass density of individual microtubules has been reported previously (Bon et al., 2014; Krivosudský et al., 2017), given the fast turnover of microtubules on the seconds timescale, the mass density of the spindle bulk might be the relevant measure in the context of spindle architecture and size control, as well as for coarse-grained modeling. However, mass density will certainly affect key cellular functions such as active and diffusive transport in the spindle, transition-state-limited reactions (Woodruff, 2018), and it will influence partitioning of macromolecules into the spindle. Equal density might support the microtubules' effect in fluidizing the mitotic cytoplasm to maintain the diffusivity and mobility of key mitotic complexes (Carlini et al., 2020). Indeed, it has been shown that the spatial arrangement of spindle microtubules can impact force generation (Shimamoto et al., 2015). Moreover, given equal density, the spindle would be neutrally buoyant, which results in a buoyant force balancing the force of gravity that would otherwise cause the spindle to sink. While in sufficiently small cells gravitational forces are considered negligible, gravity becomes increasingly significant in large amphibian eggs (Feric and Brangwynne,

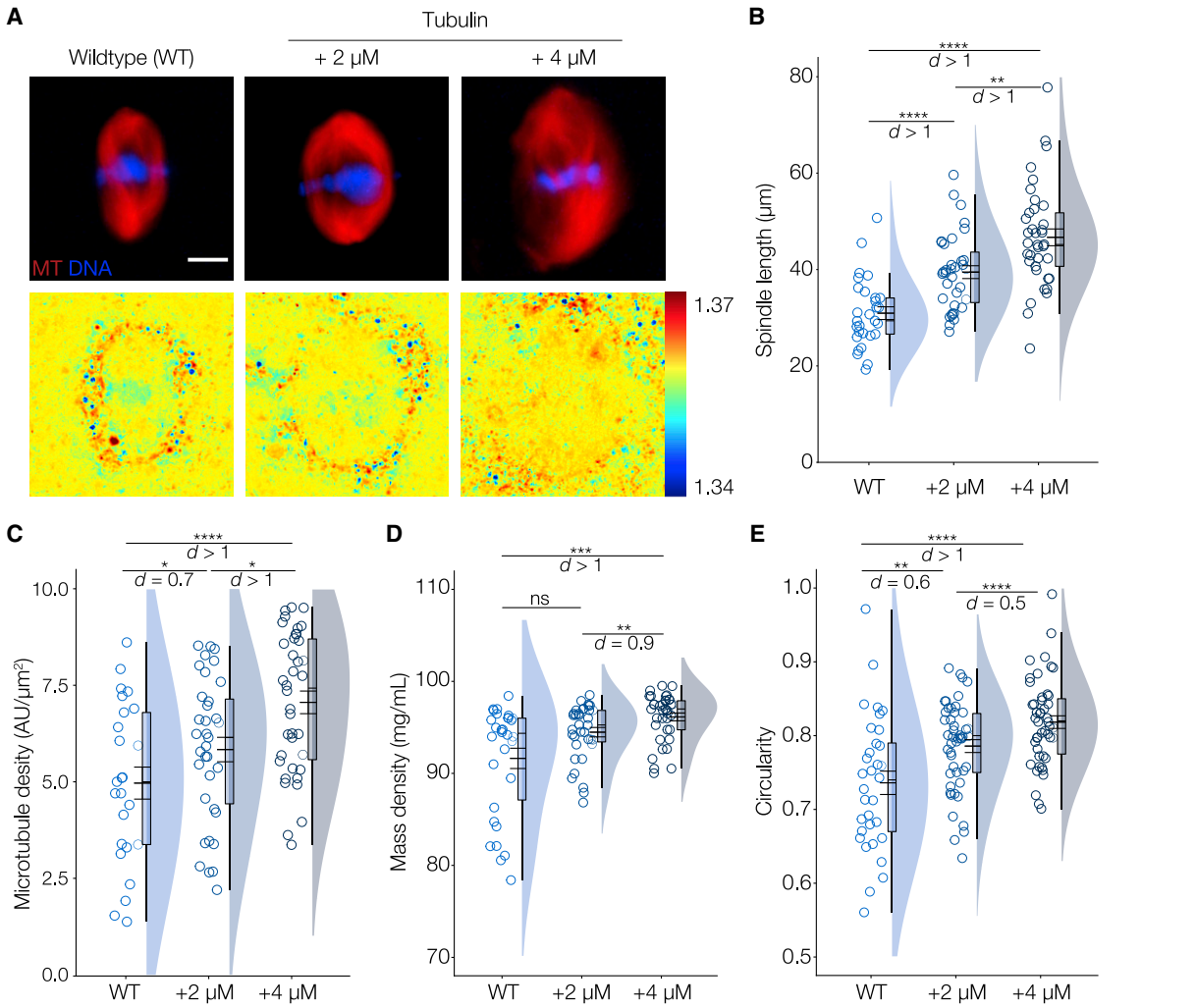

Figure 4. Increasing tubulin concentration increases spindle mass density and spindle circularity

(A) Representative fluorescence (top: red, microtubules; blue, DNA) and corresponding ODT images (bottom) of spindles with no (wild type), 2 and 4 μM additional *Xenopus* tubulin. Scale bar, 10 μm.

(B) Spindle length increases with increasing tubulin concentration (n = 29, 35, and 37 spindles from 3 independent experiments). Wild type: 31 ± 1.3 μm, +2 μM: 40 ± 1.3 μm, $p_{WT,\ 2\ \mu M} < 0.0001$, Cohen's $d_{WT,\ 2\ \mu M} > 1$, +4 μM: 47 ± 1.7 μm, $p_{WT,\ 4\ \mu M} < 0.0001$, Cohen's $d_{WT,\ 4\ \mu M} > 1$.

(C and D) (C) Microtubule density measured by tubulin fluorescence (wild type: 5 ± 0.4 AU/μm², +2 μM: 6 ± 0.3 AU/μm²; $p_{WT,\ 2\ \mu M} < 0.05$, Cohen's $d_{WT,\ 2\ \mu M} = 0.7$ and +4 μM: 7 ± 0.3 AU/μm²; $p_{WT,\ 4\ \mu M} < 0.0001$, Cohen's $d_{WT,\ 4\ \mu M} > 1$) and (D) mass density increases with increasing tubulin concentrations (wild type: 92 ± 1.1 mg/mL, +2 μM: 95 ± 0.5 mg/mL; $p_{WT,\ 2\ \mu M} > 0.05$, Cohen's $d_{WT,\ 2\ \mu M} = 0.6$ and +4 μM: 96 ± 0.4 mg/mL; $p_{WT,\ 4\ \mu M} < 0.001$, Cohen's $d_{WT,\ 4\ \mu M} = 0.9$).

(E) Supplementing tubulin alters spindle shape (as measured by the circularity shape factor, n = 33, 48, and 47 spindles from 4 independent experiments). Data are represented as mean ± SEM. Mann-Whitney test. Black bar and lines indicate mean and SEM. Box and violin plot for each condition indicated, ns $p > 0.05$, *$p < 0.05$, **$p < 0.01$, ***$p < 0.001$, and ****$p < 0.0001$. See also Figure S4.

2013). However, the spindle's mass density is not an isolated parameter but a material property that affects and is affected by a complex mix of active forces (such as motors and microtubule dynamics) and passive factors (such as elasticity and molecular friction) (Dumont and Mitchison, 2009; Elting et al., 2018).

Third, our data imply that the spindle indeed forms by demixing. As the spindle and the cytoplasm have similar densities but significantly different molecular compositions (Kaye et al., 2018), our study is in line with recent studies on intracellular, phase-separated FUS condensates, which have also been shown to have the same RI and mass density as the surrounding cytoplasm (Schlüßler et al., 2020). In a complex and crowded environment like the cytoplasm or egg extract, a simplified view of global density transitions taking place during liquid-liquid phase separation may not necessarily hold true. Instead, the composition and spatial distribution of molecules changes without impacting the local physical density (as discussed in Alberti et al., 2019). However, the relationship between molecular specificity and material properties of (phase-separating and transitioning) compartments within crowded physiologically relevant solvents such as the cyto- or nucleoplasm remains an exciting topic for future research.

Limitations of this study

In this study, we measure the *Xenopus* spindle's mass density distribution using correlative fluorescence imaging and label-free three-dimensional ODT. ODT provides a 3D tomogram computed from multiple 2D quantitative phase images that are acquired upon illuminating the sample at various oblique angles. As the phase retardation in the 2D quantitative phase image is generated by the difference in the RI between the object and the surrounding medium, the absolute RI of the medium needs to be independently measured by an Abbe refractometer as a reference. Thus, for each experiment, the RI of the extract was first measured as an averaged value of the entire cytoplasm. After tomogram reconstruction (Kim et al., 2014; Müller et al., 2015), each pixel within the image was assigned a calculated RI. From this RI value, the mass density of each component (spindle, cytoplasm, chromatin, and membrane) was directly calculated since the RI value in biological samples is linearly proportional to the mass density of the material with the proportionality coefficient of RI increment α (Barer and Tkaczyk, 1954). Thus, the mass density of spindle components is sensitive to the choice of the RI increment value. To tackle this problem, we provide some molecular specificity using three-channel fluorescence to accurately identify areas enriched in microtubules (labeled with TAMRA-tubulin), chromatin (labeled with Hoechst-33342), and membranes (labeled with $DiOC_6$). We then use the appropriate α for each region: for the spindle and the cytoplasm, we use $\alpha = 0.190$ mL/g as established for proteins and nucleic acids (Zhao et al., 2011; Krivosudský et al., 2017) and $\alpha = 0.135$ mL/g for membranes (Mashaghi et al., 2008). While *Xenopus* egg extracts are a complex mixture of macromolecules (including proteins, nucleic acids, glycogen, and lipids), choosing a specific α is the present limitation of our approach. In order to include sugars ($\alpha = 0.15$ mL/g; Zangle and Teitell, 2014) or lipids ($\alpha = 0.135$ mL/g), we would need to know their exact proportion in extracts. In the future, a combined optical approach of Raman imaging with ODT could help resolve this shortcoming. The Raman spectrum could first be used to identify the composition of chemical species contained within a given voxel, and then the appropriate α value could be used to extract the correct mass density from the RI values measured by ODT.

STAR★METHODS

Detailed methods are provided in the online version of this paper and include the following:

- KEY RESOURCES TABLE
- RESOURCE AVAILABILITY
  - Lead contact
  - Material availability
  - Data and code availability
- EXPERIMENTAL MODEL AND SUBJECT DETAILS
  - *Xenopus laevis*
- METHOD DETAILS
  - Spindle assembly in *Xenopus laevis* egg extracts
  - Image acquisition via correlative epifluorescence-ODT setup
  - Analysing ODT and fluorescence images
  - Mass density and microtubule density in different spindle regions
  - Calculating microtubule mass and spindle dry mass
  - Spindle shape analysis
  - RI measurements made via ODT match RI values obtained with a refractometer (Related to Figure S1)
  - Optical stretcher experiments on spindles confirm refractive index observations (Related to Figure S2)
  - Membranes surrounding spindles have a high RI (Related to Figure S3)
  - Tubulin addition does not increase the refractive index of the cytoplasm (Related to Figure S4)
- QUANTIFICATION AND STATISTICAL ANALYSIS

SUPPLEMENTAL INFORMATION

Supplemental information can be found online at https://doi.org/10.1016/j.devcel.2021.03.013.

ACKNOWLEDGMENTS

The authors thank past and current members of the Guck and Reber labs, Jan Brugués for helpful discussions and the provision of *Xenopus* egg extract, Heino Andreas for maintaining the frogs and Jan Schmoranzer from the Advanced Medical BIOimaging Core Facility, Charité Berlin. The authors acknowledge funding from the Alexander von Humboldt Foundation (AvH professorship to J.G.), the Volkswagen Foundation (research grant 92847 to J.G.) and the DFG (RE 3925/1-1 to S.R.). S.R. also acknowledges funding by the IRI Life Sciences (Humboldt-Universität zu Berlin, Excellence Initiative/DFG).

AUTHOR CONTRIBUTIONS

A.B. and S.R. conceived the project. K.K. designed and developed the correlative fluorescence-ODT setup. G.C. optimized the OS for *Xenopus* egg extracts. A.B. performed spindle assembly reactions and purified tubulin. K.K. and A.B. performed experiments involving ODT and fluorescence microscopy. K.K. developed the script for field retrieval and tomogram reconstruction. A.B. and K.K. analyzed the data. A.B. and S.R. wrote the manuscript with input from K.K. and J.G.

DECLARATION OF INTERESTS

The authors declare no competing interests.

INCLUSION AND DIVERSITY

One or more of the authors of this paper self-identifies as an underrepresented ethnic minority in science. One or more of the authors of this paper self-identifies as living with a disability. The author list of this paper includes contributors from the location where the research was conducted who participated in the data collection, design, analysis, and/or interpretation of the work.

Received: November 10, 2020
Revised: January 11, 2021
Accepted: March 8, 2021
Published: April 5, 2021

REFERENCES

Abuhattum, S., Kim, K., Franzmann, T.M., Eßlinger, A., Midtvedt, D., Schlüßler, R., Möllmert, S., Kuan, H., Alberti, S., Zaburdaev, V., and Guck, J. (2018). Intracellular mass density increase is accompanying but not sufficient for stiffening and growth arrest of yeast cells. Front. Phys. *6*, 131.

Alberti, S., Gladfelter, A., and Mittag, T. (2019). Considerations and challenges in studying liquid-liquid phase separation and biomolecular condensates. Cell *176*, 419–434.

Allen, M., Poggiali, D., Whitaker, K., Marshall, T.R., and Kievit, R.A. (2019). Raincloud plots: a multi-platform tool for robust data visualization. Wellcome Open Res. *4*, 63.

Ashby, M.F. (2011). Materials Selection in Mechanical Design, Fourth Edition (Elsevier Science).

Barer, R., Ross, K.F.A., and Tkaczyk, S. (1953). Refractometry of living cells. Nature *171*, 720–724.

Barer, R., and Tkaczyk, S. (1954). Refractive index of concentrated protein solutions. Nature *173*, 821–822.

Bon, P., Lécart, S., Fort, E., and Lévêque-Fort, S. (2014). Fast label-free cytoskeletal network imaging in living mammalian cells. Biophys. J. *106*, 1588–1595.

Brugués, J., and Needleman, D. (2014). Physical basis of spindle self-organization. Proc. Natl. Acad. Sci. USA *111*, 18496–18500.

Carlini, L., Brittingham, G.P., Holt, L.J., and Kapoor, T.M. (2020). Microtubules enhance mesoscale effective diffusivity in the crowded metaphase cytoplasm. Dev. Cell *54*, 574–582.e4.

Crowder, M.E., Strzelecka, M., Wilbur, J.D., Good, M.C., von Dassow, G., and Heald, R. (2015). A comparative analysis of spindle morphometrics across metazoans. Curr. Biol. *25*, 1542–1550.

Dalton, C.M., and Carroll, J. (2013). Biased inheritance of mitochondria during asymmetric cell division in the mouse oocyte. J. Cell Sci. *126*, 2955–2964.

Decker, F., Oriola, D., Dalton, B., and Brugués, J. (2018). Autocatalytic microtubule nucleation determines the size and mass of Xenopus laevis egg extract spindles. eLife *7*, e31149.

Dumont, S., and Mitchison, T.J. (2009). Force and length in the mitotic spindle. Curr. Biol. *19*, R749–R761.

Elting, M.W., Suresh, P., and Dumont, S. (2018). The spindle: integrating architecture and mechanics across scales. Trends Cell Biol *28*, 896–910.

Feric, M., and Brangwynne, C.P. (2013). A nuclear F-actin scaffold stabilizes ribonucleoprotein droplets against gravity in large cells. Nat. Cell Biol. *15*, 1253–1259.

Gardner, M.K., Zanic, M., Gell, C., Bormuth, V., and Howard, J. (2011). Depolymerizing kinesins Kip3 and MCAK shape cellular microtubule architecture by differential control of catastrophe. Cell *147*, 1092–1103.

Gatlin, J.C., Matov, A., Groen, A.C., Needleman, D.J., Maresca, T.J., Danuser, G., Mitchison, T.J., and Salmon, E.D. (2009). Spindle fusion requires dynein-mediated sliding of oppositely oriented microtubules. Curr. Biol. *19*, 287–296.

Good, M.C., Vahey, M.D., Skandarajah, A., Fletcher, D.A., and Heald, R. (2013). Cytoplasmic volume modulates spindle size during embryogenesis. Science *342*, 856–860.

Grenfell, A.W., Strzelecka, M., Crowder, M.E., Helmke, K.J., Schlaitz, A.L., and Heald, R. (2016). A versatile multivariate image analysis pipeline reveals features of Xenopus extract spindles. J. Cell Biol. *213*, 127–136.

Groen, A.C., Coughlin, M., and Mitchison, T.J. (2011). Microtubule assembly in meiotic extract requires glycogen. Mol. Biol. Cell *22*, 3139–3151.

Guck, J., Ananthakrishnan, R., Mahmood, H., Moon, T.J., Cunningham, C.C., and Käs, J. (2001). The optical stretcher: a novel laser tool to micromanipulate cells. Biophys. J. *81*, 767–784.

Guck, J., Schinkinger, S., Lincoln, B., Wottawah, F., Ebert, S., Romeyke, M., Lenz, D., Erickson, H.M., Ananthakrishnan, R., Mitchell, D., et al. (2005). Optical deformability as an inherent cell marker for testing malignant transformation and metastatic competence. Biophys. J. *88*, 3689–3698.

Guillén-Boixet, J., Kopach, A., Holehouse, A.S., Wittmann, S., Jahnel, M., Schlüßler, R., Kim, K., Trussina, I.R.E.A., Wang, J., Mateju, D., et al. (2020). RNA-induced conformational switching and clustering of G3BP drive stress granule assembly by condensation. Cell *181*, 346–361.e17.

Hannak, E., and Heald, R. (2006). Investigating mitotic spindle assembly and function in vitro using Xenopus laevis egg extracts. Nat. Protoc. *1*, 2305–2314.

Hirst, W.G., Biswas, A., Mahalingan, K.K., and Reber, S. (2020). Differences in intrinsic tubulin dynamic properties contribute to spindle length control in Xenopus species. Curr. Biol. *30*, 2184–2190.e5.

Huster, C., Rekhade, D., Hausch, A., Ahmed, S., Hauck, N., Thiele, J., Guck, J., Kroy, K., and Cojoc, G. (2020). Stretching and heating cells with light—nonlinear photothermal cell rheology. New J. Phys. *22*, 085003.

Hyman, A.A., Weber, C.A., and Jülicher, F. (2014). Liquid-liquid phase separation in biology. Annu. Rev. Cell Dev. Biol. *30*, 39–58.

Jiang, H., Wang, S., Huang, Y., He, X., Cui, H., Zhu, X., and Zheng, Y. (2015). Phase transition of spindle-associated protein regulate spindle apparatus assembly. Cell *163*, 108–122.

Kaye, B., Stiehl, O., Foster, P.J., Shelley, M.J., Needleman, D.J., and Fürthauer, S. (2018). Measuring and modeling polymer concentration profiles near spindle boundaries argues that spindle microtubules regulate their own nucleation. New J. Phys. *20*, 055012.

Kim, D., Lee, S., Lee, M., Oh, J., Yang, S.A., and Park, Y. (2018). Holotomography: refractive index as an intrinsic imaging contrast for 3-D label-free live cell imaging. bioRxiv. https://doi.org/10.1101/106328.

Kim, K., and Guck, J. (2020). The relative densities of cell cytoplasm, nucleoplasm, and nucleoli are robustly conserved during cell cycle and drug perturbations. Biophys. J. *119*, 1946–1957.

Kim, K., Yoon, H., Diez-Silva, M., Dao, M., Dasari, R.R., and Park, Y. (2014). High-resolution three-dimensional imaging of red blood cells parasitized by Plasmodium falciparum and in situ hemozoin crystals using optical diffraction tomography. J. Biomed. Opt. *19*, 011005.

Kim, K., Yoon, J., Shin, S., Lee, S., Yang, S.A., and Park, Y. (2016). Optical diffraction tomography techniques for the study of cell pathophysiology. J. Biomed. Photonics Eng. *2*, 020201.

King, M.R., and Petry, S. (2020). Phase separation of TPX2 enhances and spatially coordinates microtubule nucleation. Nat. Commun. *11*, 270.

Krivosudský, O., Dráber, P., and Cifra, M. (2017). Resolving controversy of unusually high refractive index of a tubulin. EPL *117*, 38003.

Lautenschläger, F., Paschke, S., Schinkinger, S., Bruel, A., Beil, M., and Guck, J. (2009). The regulatory role of cell mechanics for migration of differentiating myeloid cells. Proc. Natl. Acad. Sci. USA *106*, 15696–15701.

Mashaghi, A., Swann, M., Popplewell, J., Textor, M., and Reimhult, E. (2008). Optical anisotropy of supported lipid structures probed by waveguide spectroscopy and its application to study of supported lipid bilayer formation kinetics. Anal. Chem. *80*, 3666–3676.

McCall, P.M., Kim, K., Fritsch, A.W., Iglesias-Artola, J.M., Jawerth, L.M., Wang, J., and Alberti, S. (2020). Quantitative phase microscopy enables precise and efficient determination of biomolecular condensate composition. bioRxiv. https://doi.org/10.1101/2020.10.25.352823.

Mitchison, T.J. (2019). Colloid osmotic parameterization and measurement of subcellular crowding. Mol. Biol. Cell *30*, 173–180.

Müller, P., Schürmann, M., and Guck, J. (2015). The theory of diffraction tomography. arXiv https://arxiv.org/abs/1507.00466.

Oriola, D., Jülicher, F., and Brugués, J. (2020). Active forces shape the metaphase spindle through a mechanical instability. Proc. Natl. Acad. Sci. USA *117*, 16154–16159.

Popescu, G., Park, Y., Lue, N., Best-Popescu, C., Deflores, L., Dasari, R.R., Feld, M.S., and Badizadegan, K. (2008). Optical imaging of cell mass and growth dynamics. Am. J. Physiol. Cell Physiol. *295*, C538–C544.

Prevedel, R., Diz-Muñoz, A., Ruocco, G., and Antonacci, G. (2019). Brillouin microscopy: an emerging tool for mechanobiology. Nat. Methods *16*, 969–977.

Reber, S., and Hyman, A.A. (2015). Emergent properties of the metaphase spindle. Cold Spring Harbor Perspect. Biol. *7*, a015784.

Reber, S.B., Baumgart, J., Widlund, P.O., Pozniakovsky, A., Howard, J., Hyman, A.A., and Jülicher, F. (2013). XMAP215 activity sets spindle length by controlling the total mass of spindle microtubules. Nat. Cell Biol. *15*, 1116–1122.

Reusch, S., Biswas, A., Hirst, W.G., and Reber, S. (2020). Affinity purification of label-free tubulins from Xenopus egg extracts. STAR Protoc. *1*, 100151.

Rieckhoff, E.M., Berndt, F., Elsner, M., Golfier, S., Decker, F., Ishihara, K., and Brugués, J. (2020). Spindle scaling is governed by cell boundary regulation of microtubule nucleation. Curr. Biol. *30*, 4973–4983.e10.

Scarcelli, G., Polacheck, W.J., Nia, H.T., Patel, K., Grodzinsky, A.J., Kamm, R.D., and Yun, S.H. (2015). Noncontact three-dimensional mapping of

intracellular hydromechanical properties by Brillouin microscopy. Nat. Methods *12*, 1132–1134.

Schindelin, J., Arganda-Carreras, I., Frise, E., Kaynig, V., Longair, M., Pietzsch, T., Preibisch, S., Rueden, C., Saalfeld, S., Schmid, B., et al. (2012). Fiji: an open-source platform for biological-image analysis. Nat. Methods *9*, 676–682.

Schlüßler, R., Kim, K., Nötzel, M., Taubenberger, A.V., Abuhattum, S., Beck, T., and Hermann, A. (2020). Combined fluorescence, optical diffraction tomography and Brillouin microscopy. bioRxiv. https://doi.org/10.1101/2020.10.30.361808.

Schweizer, N., Pawar, N., Weiss, M., and Maiato, H. (2015). An organelle-exclusion envelope assists mitosis and underlies distinct molecular crowding in the spindle region. J. Cell Biol. *210*, 695–704.

Shimamoto, Y., Forth, S., and Kapoor, T.M. (2015). Measuring pushing and braking forces generated by ensembles of kinesin-5 crosslinking two microtubules. Dev. Cell *34*, 669–681.

Shimamoto, Y., Maeda, Y.T., Ishiwata, S.I., Libchaber, A.J., and Kapoor, T.M. (2011). Insights into the micromechanical properties of the metaphase spindle. Cell *145*, 1062–1074.

So, C., Seres, K.B., Steyer, A.M., Mönnich, E., Clift, D., Pejkovska, A., Möbius, W., and Schuh, M. (2019). A liquid-like spindle domain promotes acentrosomal spindle assembly in mammalian oocytes. Science *364*, eaat9557.

Sung, Y., Choi, W., Fang-Yen, C., Badizadegan, K., Dasari, R.R., and Feld, M.S. (2009). Optical diffraction tomography for high resolution live cell imaging. Opt. Express *17*, 266–277.

Takagi, J., Itabashi, T., Suzuki, K., Kapoor, T.M., Shimamoto, Y., and Ishiwata, S.I. (2013). Using micromanipulation to analyze control of vertebrate meiotic spindle size. Cell Rep. *5*, 44–50.

Takagi, J., Sakamoto, R., Shiratsuchi, G., Maeda, Y.T., and Shimamoto, Y. (2019). Mechanically distinct microtubule arrays determine the length and force response of the meiotic spindle. Dev. Cell *49*, 267–278.e5.

Wegst, U.G.K., and Ashby, M.F. (2004). The mechanical efficiency of natural materials. Philos. Mag. *84*, 2167–2186.

Widlund, P.O., Podolski, M., Reber, S., Alper, J., Storch, M., Hyman, A.A., Howard, J., and Drechsel, D.N. (2012). One-step purification of assembly-competent tubulin from diverse eukaryotic sources. Mol. Biol. Cell *23*, 4393–4401.

Wieczorek, M., Bechstedt, S., Chaaban, S., and Brouhard, G.J. (2015). Microtubule-associated proteins control the kinetics of microtubule nucleation. Nat. Cell Biol. *17*, 907–916.

Wolf, E. (1969). Three-dimensional structure determination of semi-transparent objects from holographic data. Opt. Commun. *1*, 153–156.

Woodruff, J.B. (2018). Assembly of mitotic structures through phase separation. J. Mol. Biol. *430*, 4762–4772.

Woodruff, J.B., Ferreira Gomes, B.F., Widlund, P.O., Mahamid, J., Honigmann, A., and Hyman, A.A. (2017). The centrosome is a selective condensate that nucleates microtubules by concentrating tubulin. Cell *169*, 1066–1077.e10.

Wühr, M., Chen, Y., Dumont, S., Groen, A.C., Needleman, D.J., Salic, A., and Mitchison, T.J. (2008). Evidence for an upper limit to mitotic spindle length. Curr. Biol. *18*, 1256–1261.

Zangle, T.A., and Teitell, M.A. (2014). Live-cell mass profiling: an emerging approach in quantitative biophysics. Nat. Methods *11*, 1221–1228.

Zhao, H., Brown, P.H., and Schuck, P. (2011). On the distribution of protein refractive index increments. Biophys. J. *100*, 2309–2317.

STAR★METHODS

KEY RESOURCES TABLE

REAGENT or RESOURCES	SOURCE	IDENTIFIER
Chemicals, Peptides, and Recombinant Proteins		
cOmplete™, EDTA-free Protease Inhibitor Cocktail	Sigma-Aldrich	Cat #: 11873580001
Pregnant mare serum gonadotropin, PMSG	MSD, Tiergesundheit	Intergonan ® 240 IU/ml
Human chorionic gonadotropin, HCG	Sigma-Aldrich	Cat #: CG-10
Cytochalasin D	Sigma-Aldrich	Cat #: C8273
Xenopus laevis egg tubulin	Hirst et al., 2020	N/A
5-TAMRA (5-Carboxytetramethylrhodamine) dye	Thermo-Fisher	Cat #: C6121
5-TAMRA labelled porcine tubulin	Reusch et al., 2020	N/A
Hoechst 33342	Thermo-Fisher	Cat #: H21492
$DiOC_6$ (3,3′-dihexyloxacarbocyanine iodide) dye	Sigma-Aldrich	Cat #: 318426
Bovine serum albumin	Sigma-Aldrich	Cat #: A2153
Piperazine-1,4-bis(2-ethanesulfonic acid) (PIPES)	Sigma-Aldrich	Cat #: P1851
EGTA	Sigma-Aldrich	Cat #: E3889
Calcium chloride dihydrate ($CaCl_2 \cdot 2H_2O$)	Carl Roth	Cat #: HN04.3
L-Cysteine	Carl Roth	Cat #: 1693.3
Magnesium chloride hexahydrate ($MgCl_2 \cdot 6H_2O$)	Carl Roth	Cat #: HN03.2
Novec 7500 fluid	3M	Cat #: 3M-ID 71-0002-5016
Mineral oil 1	Cargille	Cat #: 1803Y series AAA
Mineral oil 2	Sigma-Aldrich	Cat #: M8410
GTP	Sigma-Aldrich	Cat #: G8877
ATP	Sigma-Aldrich	Cat #: A26209
Ammonium sulfate ($(NH_4)_2SO_4$)	Carl Roth	Cat #: 3746.1
Critical Commercial Columns and Consumables		
TOG1/2-column	Widlund et al. 2012	N/A
HiTrap™ NHS-activated HP column (5 mL)	GE Healthcare	Cat #: GE17-0717-01
PD-10 desalting columns	GE Healthcare	Cat #: 17085101
Amicon Ultra-4 Centrifugal filter, 30 kDa (0.5 mL)	Merck Millipore	Cat #: UFC5030
Experimental Models: Organisms/Strains		
Xenopus laevis	Nasco	Cat #: LM00535
Other – Equipment		
Glass coverslips	VWR	Cat #: 631-1573P
Correlative ODT-Epifluorescence microscope	Kim and Guck, 2020; this study	N/A
Optical stretcher	Guck et al., 2001; this study	N/A
Microcapillary manipulator	Eppendorf	Cat #: InjectMan 2
Abbe refractometer	Arcada	Cat #: ABBE-2WAJ
Software and Algorithms		
FIJI	Schindelin et al., 2012	N/A
Matlab R 2019b	The MathWorks	https://de.mathworks.com/

(*Continued on next page*)

Continued

REAGENT or RESOURCES	SOURCE	IDENTIFIER
Prism version 8.0 for Mac OS X	GraphPad	https://www.graphpad.com/
Raincloud plots Shiny app	Allen et al., 2019	https://gabrifc.shinyapps.io/raincloudplots
ODT reconstruction algorithm	This study	https://github.com/OpticalDiffractionTomography/ODT_Reconstruction_Extract

RESOURCE AVAILABILITY

Lead contact

Further information and requests for resources and reagents should be directed to and will be fulfilled by the Lead Contact, Simone Reber (simone.reber@iri-lifesciences.de). Further information and requests concerning ODT and OS should be directed to and will be fulfilled by Jochen Guck (jochen.guck@mpl.mpg.de).

Material availability

This study did not generate new unique reagents.

Data and code availability

The code utilized in this study to reconstruct RI tomograms is publicly available online at https://github.com/OpticalDiffractionTomography/ODT_Reconstruction_Extract Please contact KK or AB for any further information regarding the code.

EXPERIMENTAL MODEL AND SUBJECT DETAILS

Xenopus laevis

The *Xenopus* frogs (adult females) used in this study are part of the *Xenopus* colony maintained at the animal husbandry of the Humboldt-Universität zu Berlin and were obtained from NASCO (Fort Atkinson, WI). *Xenopus* frogs were maintained in a recirculating tank system with regularly monitored temperature and water quality (pH, conductivity, and nitrate/nitrite levels) at a temperature of 18-20°C. Frogs were fed with food pellets (V7106-0202) from ssniff Spezialdiäten GmbH. All experimental protocols involving frogs were performed in accordance with national regulatory standards and ethical rules and reviewed and approved by the LaGeSo under Reg.-Nr. 0096/15.

METHOD DETAILS

Spindle assembly in *Xenopus laevis* egg extracts

Cytostatic factor (CSF) extracts were prepared from *Xenopus* eggs arrested in metaphase of meiosis II as described previously (Hannak and Heald, 2006). In brief, *X. laevis* frogs were primed with 100 U of pregnant mare serum gonadotrophin (PMSG) 3-7 days before the experiment and were boosted with 1000 U human chorionic gonadotrophin (HCG) to induce egg laying. Eggs arrested in the metaphase stage of meiosis II were collected, dejellied using L-Cysteine and fractionated via centrifugation. The cytoplasmic layer was isolated and supplemented with Cytochalasin and Complete EDTA-free protease inhibitor. To promote bipolar spindle formation, demembranated sperm nuclei were added to the CSF-extract. Cycling to interphase was induced by the addition of $CaCl_2$ to 0.6 mM and after 90 min the system was rearrested in M-phase using one volume of CSF-extract. Brain tubulin labelled with 5-Carboxytetramethylrhodamine (5-TAMRA, C6121 Thermo-Fisher) was supplemented to the extracts (0.1mg/mL) to visualise spindles. To image spindles, 6 μl of the extract were pipetted onto a clean glass coverslip (631-1573P, VWR International). Another coverslip was immediately placed on this coverslip to create a squashed egg extract sample, which provided a thin layer that could be easily imaged with our imaging setup. For the tubulin addition assays, assembly-competent *X. laevis* tubulin was purified using a TOG-column as in (Widlund et al., 2012; Reusch et al., 2020). In brief, the extract was first diluted with an equal volume of BRB80 buffer (80 mM PIPES, 1 mM EGTA, 1 mM $MgCl_2$, pH 6.9) and centrifuged at 80,000 rpm in an MLA-80 rotor (Beckman-Coulter) for 10 min at 4°C. The supernatant was cycled through a 5 mL HiTrap NHS-activated HP column (GE Healthcare) coupled with a fusion protein of GST and TOG domains 1 and 2 of *S. cerevisiae* Stu2 (GST-TOG1/2) at 0.5 column volumes per minute (CV/min) for 20 min. The column was washed with 8 CV of BRB80 supplemented with 100 mM Mg^{2+} GTP (wash buffer) followed by 3 CV of BRB80 supplemented with 10 mM $MgCl_2$ and 5 mM ATP and incubated for 15 min to induce dissociation of chaperone proteins. The column was then washed with 3 CV BRB80/ATP buffer and 20 CV of wash buffer. Tubulin was eluted at 1 mL/min with wash buffer supplemented with 0.5 M $(NH_4)_2SO_4$. Peak fractions were determined by measuring A_{280} values with a NanoDrop spectrophotometer (Thermo), pooled, buffer-exchanged into BRB80 containing 10 mM Mg^{2+} GTP using PD10 desalting columns (GE Healthcare) and concentrated to at least 30 mM using a concentration filter column with a 30 kDa cut-off (Amicon). Concentrated tubulin was incubated on ice for 30 min to fully depolymerize microtubules, centrifuged for 15 min at 2°C in a TLA-100 rotor at 80,000 rpm, aliquoted into 5 or 10 μL

single-use aliquots, and snap-frozen in liquid nitrogen. For the assay, steady-state spindles were first assembled as described above. Tubulin was added to pre-assembled spindles at the indicated final concentrations. The reaction was incubated for 30 minutes to allow the spindles to reach a new steady state. The added volume of tubulin containing buffer (1x BRB80: 80 mM PIPES, 1 mM EGTA, 1 mM $MgCl_2$, pH 6.9) never exceeded more than 10% of the original volume of extract. Following the incubation, 6 μl of extract containing spindles was squashed between two coverslips and imaged.

Image acquisition via correlative epifluorescence-ODT setup

Refractive index (RI) tomograms were obtained using a custom-built optical diffraction tomography microscope employing a Mach-Zehnder interferometer. The detailed description of the same optical setup can be found in (Abuhattum et al., 2018; Kim and Guck, 2020). Briefly, a coherent laser beam (λ = 532 nm) was split in two using a single-mode fiber optic coupler. One beam was used as a reference beam. The other was used as a sample beam to illuminate the sample using a tube lens (f = 175 mm) and a water-dipping objective lens (NA = 1.0, 40×, 421462-9900, Carl Zeiss AG). In order to reconstruct a 3D RI tomogram of the sample, the sample was illuminated from 150 different incident angles by a dual-axis galvano-mirror (GVS012/M, Thorlabs Inc.) covering the angular range from -48° to 48°. The scattered light from the sample was collected by a high numerical aperture objective lens (water immersion, NA = 1.2, 63×, 441777-9970, Carl Zeiss AG) and interfered with the reference beam at the image plane, which generated spatially modulated holograms. The holograms were recorded by a CCD camera (FL3-U3-13Y3M-C, FLIR Systems, Inc.). The detailed principle for tomogram reconstruction can be found in (Kim et al., 2014; Müller et al., 2015). Briefly, from the spatially modulated holograms, the complex optical fields of light diffracted by the sample were retrieved by applying a field retrieval method based on Fourier transformation. The first-order Fourier spectra information was selected by spatial filtering corresponding to numerical aperture of the objective lens. The 3D RI tomogram of the sample was reconstructed by mapping 2D Fourier spectra of the retrieved complex optical fields based on Fourier diffraction theorem (Wolf, 1969; Sung et al., 2009; Kim et al., 2014). A 2D Fourier spectrum is mapped into the surface of an Ewald sphere, and the center position of the Ewald sphere is translated in the 3D Fourier space corresponding to the spatial frequency of the incident angle. Non-negativity constraint is applied to fill the missing cone artifact. Epifluorescence imaging was performed using the same optical setup. An incoherent beam from a halogen lamp was coupled into the light path by a three-channel dichroic mirror, and the excitation and emission filters corresponding to fluorescence probes were alternated sequentially. The fluorescence emission signals were recorded by the same camera in the ODT setup with a typical exposure time of 900 milliseconds. The measured 2D fluorescence image was correlated with the cross-sectional slice of the reconstructed tomogram at z = 0 μm in order to identify chromatin and tubulin in the RI tomogram.

Analysing ODT and fluorescence images

As described above, a 3D tomogram is computed from multiple 2D quantitative phase images that are acquired upon illuminating the sample at various oblique angles. As the phase retardation in the 2D quantitative phase image is generated by the difference in the refractive index between the object and the surrounding medium, the absolute refractive index of the medium needs to be independently measured by an Abbe refractometer (Arcarda ABBE-2WAJ). Thus, for each experiment, the RI of the extract ($n_{cytoplasm}$) was first measured as an averaged value of the entire cytoplasm and set to a reference value of 100 mg/mL. After tomogram reconstruction (Kim et al., 2014; Müller et al., 2015), each pixel within the image was assigned a calculated RI. Finally, from this RI value, the mass density of each component (spindle, cytoplasm, chromatin or membrane) was directly calculated since the RI value in biological samples is linearly proportional to the mass density of material with the proportional coefficient of RI increment, α (Barer and Tkaczyk, 1954, our Figure S1). The mass density of spindles was calculated for each pixel within the central slice (z = 0) of the RI tomogram using the relationship: $n_{spindle} = n_{cytoplasm} + \alpha C_{spindle}$ (Equation 1), where $n_{spindle}$ is the average RI of the spindle, $n_{cytoplasm}$ is the RI of the extract, α is the RI increment (0.190 mL/g for proteins and nucleic acids (Zhao et al., 2011)) and $C_{spindle}$ is the mass density inside the spindle. The mean mass density of spindles, cytoplasm, and chromatin was calculated from square regions of interest (5 μm x 5 μm). For detection via epifluorescence, microtubules were labelled with 5-TAMRA porcine tubulin and chromatin was labelled with Hoechst 33342 dye. Masks of the spindle and chromatin location were generated by manually segmenting the epifluorescence image or using Otsu thresholding.

Mass density and microtubule density in different spindle regions

Spindle regions were defined as in Takagi et al. (2019). Each region was identified via fluorescence. Within these regions, ROIs (5 μm x 5 μm) were selected and transferred to the ODT image, where the mass density was calculated by averaging over the entire ROI. For the line scan, a line of defined thickness and length (5 μm x 50 μm) along the spindle's major axis was used to measure fluorescence intensity and calculate the mass density profile. To calculate microtubule density in different spindle regions, epifluorescence images were deconvolved using the built-in deconvolution function (deconvblind) in Matlab. The fluorescence images were converted into 32-bit (float) images using FIJI and normalised from 0-1 by dividing the grey value at each pixel by the maximum grey value in the deconvolved image. The microtubule density at each region was then finally calculated by dividing the total normalised fluorescence intensity value by the area of each region.

Calculating microtubule mass and spindle dry mass

To measure the total microtubule mass, grey values from normalised fluorescence images were integrated over each spindle region. Spindle height was estimated from spinning disc confocal data and ODT images to be on average 8.5 ± 0.2 μm. Spindle volume was

calculated using $\frac{4}{3}\ \pi\ abc$ (Equation 2), where *a* was half of the major axis length, *b* was half of the minor axis length and *c* was half the height of spindles. To calculate the spindle dry mass, each spindle's mass density as determined via ODT was multiplied with its volume.

Spindle shape analysis

Spindle circularity was measured by generating a mask of spindles from the epifluorescence images and then using the Circularity (C) shape descriptor in FIJI, where $C = \frac{4 * Area}{Perimeter^2}$ (Equation 3). A perfect circle has a value of 1.0 and ellipses have a shape between 0-1 with more elongated shapes having lower values.

RI measurements made via ODT match RI values obtained with a refractometer (Related to Figure S1)

To illustrate how the concentration of a protein-rich solution scales with its refractive index (RI), we used bovine serum albumin (BSA, SIGMA: A2153). A concentrated solution of BSA (140 mg/ml) in distilled water was first prepared. Next, the RI of the solution was measured with the help of an Abbe refractometer (Arcarda® ABBE-2WAJ). The BSA solution was then serially diluted to obtain the indicated final concentrations (120 mg/mL, 100 mg/mL, 80 mg/mL, 60 mg/mL, 40 mg/mL and 20 mg/mL) and the RI was measured with the refractometer. This experiment was repeated three times to account for experimental variability. The RI increment (α, d*n*/d*C*) calculated from Figure S1A was 0.19 mL/g. This value is similar to other experimental and theoretical measurements of the RI increment of proteins (Zhao et al., 2011).

To test whether ODT reliably provides quantitative RI information, we performed experiments using BSA solutions and mineral oil droplets resuspended in *Xenopus* egg extract. First, we imaged BSA solutions (ranging from 0 mg/mL to 140 mg/mL, Figures S1B and S1C) with ODT and compared the calculated RI values to those measured by the refractometer. We found that ODT provides the same RI value with minimal error (0.007-0.029%, indicated in Figure S1B). Next, to test the accuracy of our ODT setup in a more complex solution, we used two different mineral oil mixtures that were dissolved in extract. Oil 1 (mixture of 3M Novec 7500 fluid and Cargille 1803Y series AAA oil) had an RI of 1.36 (via refractometer) and oil 2 (Sigma: M8410) had an RI of 1.467 (via refractometer, also the manufacturer value). 2 μl of mineral oil were mixed with 10 μl of extract. Mineral oil does not dissolve in extract and maintains its integrity in suspended oil droplets. 6 μl of this mixture were squashed between two coverslips. ODT images of single droplets of each oil surrounded by extract as shown in Figure S1D were acquired. The RI of extract was measured using an Abbe refractometer and used as a reference. The ODT tomograms were reconstructed using the field retrieval and tomogram reconstruction algorithm, and the RI of oil in individual droplets was back calculated (Figure S1E). We found that our technique was able to recapitulate the RI of each oil with low error (0.2% for oil 1 and 0.9% for oil 2). Quantification of RI in both cases was done using FIJI and statistical analysis was performed using GraphPad Prism.

Optical stretcher experiments on spindles confirm refractive index observations (Related to Figure S2)

To further validate our observations that the RI of the spindle is similar to the surrounding cytoplasm in *Xenopus* egg extracts, we employed an optical stretcher (Guck et al., 2001) setup that was optimised to make measurements in extracts (Figure S2A). The optical stretcher (OS) consists of counter-propagating laser beams that can be used to trap and deform (stretch) soft matter. Its working principle is based on surface forces that arise upon the transfer of photon momentum as light passes through materials that are of different RI values. The higher the RI difference between the object and the surrounding medium, the stronger the optical forces acting on the object and the more effective the optical trapping. When the laser power is increased, a stably trapped object is stretched due to an increase in the outward pointing optical forces acting on the object's surface. Upon reducing the power back to the trapping level, a fully elastic object should relax back to its original size and shape. We were able to successfully trap and deform a vesicle (Figure S2B, 25 μm in diameter) in *Xenopus* egg extract using a trapping power of 0.3 W and a stretching power of 0.65 W. When spindles (labelled with TAMRA-tubulin) were placed in the middle of the trapping region (Figure S2C, with the same trapping power as for the vesicle) with the help of a microcapillary manipulator (Eppendorf InjectMan 2), the structure remained steady without any movement for 20 seconds. Upon increasing the power to 0.65 W (maximum value possible with the coupled diode lasers, Lumics LU0808M250) no effect was observed on the spindle. Further, no change in spindle geometry or length (no deformation) was observed upon maintaining the high power on for an additional 20 seconds. Our experiments show that vesicles in extract can be deformed using our custom optical stretcher. Spindles, however, experience only weak or no forces. This observation can be explained as a consequence of the RI of spindles being very similar to that of the extract and thus confirm our ODT measurements.

Membranes surrounding spindles have a high RI (Related to Figure S3)

To label membranes in *Xenopus* egg extracts, we added $DiOC_6$ dye (SIGMA: 318426, 100 μM final concentration). Membranes were visualised using epifluorescence illumination and appropriate excitation and emission filters for the probe (Figure S3B). Square regions of interest (5 μm x 5 μm) were recorded from the fluorescence images and transferred to the ODT image (Figure S3C). The average RI was determined using FIJI. Mass density of membranes was calculated using equation (1) with an α value for lipids (0.135 mL/g; Mashaghi et al., 2008). A quantification of the RI and mass density of different ROIs is provided in Figure S3D.

Tubulin addition does not increase the refractive index of the cytoplasm (Related to Figure S4)

To check whether adding tubulin increased the overall RI of the extract, we measured the RI of 150 random ROIs (5 μm x 5 μm) from 3 independent experiments. As illustrated in Figure S4A, tubulin addition did not impact the overall RI of the cytoplasm.

QUANTIFICATION AND STATISTICAL ANALYSIS

In each figure legend, details about the quantifications are provided, including the number of events/spindles measured (n), the mean/median values, and the SEM/quartiles. In addition, information about the statistical tests used for measuring significance, effect size and their interpretation is provided. For statistical analysis and plotting, we utilised GraphPad Prism version 8.0 for Mac OS X, GraphPad Software, La Jolla California USA, www.graphpad.com and the online GUI-interface to create Raincloud plots (Allen et al., 2019), https://gabrifc.shinyapps.io/raincloudplots/. The alpha value was set at 0.05 and the *p* value was calculated to test how different the groups were from each other. *P value*s greater than 0.05 are represented by "ns". A single * indicates a *p* value $\leq$ 0.05, ** indicates *p* values $\leq$ 0.01, *** indicates *p* values $\leq$ 0.001, and **** indicates *p* values $\leq$ 0.0001. In addition to the significance, we also indicate the effect size by calculating Cohen's *d*. An effect size between 0.20 – 0.50 was considered small, while effect sizes between 0.51 – 0.80 were considered medium and d > 0.81 was considered large. For the linear fits, bold lines indicate the best fit and thin/dotted lines indicate the 95% confidence interval. R^2 values indicated for each fit. When necessary, graph visuals such as line thickness, fonts, and colours were optimised using Adobe Illustrator.